Chemical
Science

EDGE ARTICLE

View Article Online
View Journal | View Issue

Cite this: *Chem. Sci.*, 2024, **15**, 7659

All publication charges for this article have been paid for by the Royal Society of Chemistry

Halogen-bonded charge-transfer co-crystal scintillators for high-resolution X-ray imaging†

Yu-Hua Chen,[a] Guo-Zhen Zhang,[a] Fu-Hai Chen,[a] Shu-Quan Zhang,[c] Xin Fang,*[a] Hong-Ming Chen*[b] and Mei-Jin Lin*[ab]

The development of high-quality organic scintillators encounters challenges primarily associated with the weak X-ray absorption ability resulting from the presence of low atomic number elements. An effective strategy involves the incorporation of halogen-containing molecules into the system through co-crystal engineering. Herein, we synthesized a highly fluorescent dye, 2,5-di(4-pyridyl)thiazolo[5,4-*d*]thiazole (Py_2TTz), with a fluorescence quantum yield of 12.09%. Subsequently, Py_2TTz was co-crystallized with 1,4-diiodotetrafluorobenzene (I_2F_4B) and 1,3,5-trifluoro-2,4,6-triiodobenzene (I_3F_3B) obtaining $Py_2TTz–I_2F_4$ and $Py_2TTz–I_3F_3$. Among them, $Py_2TTz–I_2F_4$ exhibited exceptional scintillation properties, including an ultrafast decay time (1.426 ns), a significant radiation luminescence intensity (146% higher than $Bi_3Ge_4O_{12}$), and a low detection limit (70.49 nGy s^{-1}), equivalent to 1/78th of the detection limit for medical applications (5.5 μGy s^{-1}). This outstanding scintillation performance can be attributed to the formation of halogen-bonding between I_2F_4B and Py_2TTz. Theoretical calculations and single-crystal structures demonstrate the formation of halogen-bond-induced rather than π–π-induced charge-transfer cocrystals, which not only enhances the X-ray absorption ability and material conductivity under X-ray exposure, but also constrains molecular vibration and rotation, and thereby reducing non-radiative transition rate and sharply increasing its fluorescence quantum yields. Based on this, the flexible X-ray film prepared based on $Py_2TTz–I_2F_4$ achieved an ultrahigh spatial resolution of 26.8 lp per mm, underscoring the superiority of this strategy in developing high-performance organic scintillators.

Received 31st January 2024
Accepted 14th April 2024

DOI: 10.1039/d4sc00735b

rsc.li/chemical-science

Introduction

Scintillators are a type of luminescent materials used to detect high-energy rays (such as X-rays, γ-rays, *etc.*), making them widely applicable in medical diagnostics, security detection, and various other fields.[1–3] Broadly, X-ray scintillators can be categorized into inorganic scintillators (*e.g.*, NaI : Tl, CsI : Tl, $PbWO_4$ and $Bi_3Ge_4O_{12}$) and organic scintillators (*e.g.*, anthracene, plastic scintillators, *etc.*).[4,5] Inorganic scintillators generally exhibit the advantages of high light yield and high X-ray absorption efficiency, but they are hindered by challenges associated with high growth temperatures and processing difficulties.[6,7] In recent years, organic scintillators have attracted significant attention due to their inherent advantages of mild synthesis temperature, low cost, and mechanical flexibility.[8–10] Nonetheless, pure organic compounds, predominantly composed of low atomic number (Z) elements such as carbon, hydrogen and nitrogen, encounter practical application challenges due to their weak X-ray attenuation coefficient and low scintillation performance.[8,11]

To overcome the challenge of low X-ray absorption efficiency in pure organic scintillators, a strategy involves the incorporation of halogen-heavy atoms into organic dyes, leading to the formation of covalent bonds through halogen substitution.[12,13] In 2020, Wang *et al.* reported on halogen-substituted phosphorescent scintillators, discovering that the heavy atom effect increased the spin-orbital coupling (SOC) of the system, enhancing the exciton utilization efficiency and thereby improving the scintillation performance of organic materials.[14] Recently, Ma *et al.*[15] and Wang *et al.*[16] successfully synthesized halogen-substituted thermally activated delayed fluorescence (TADF) materials, achieving an enhancement in radiation luminescence (RL) intensity compared to their non-halogenated counterparts. However, a balance between high X-ray absorption, high scintillation performance and ultrafast decay time proves challenging due to the intrinsic luminescent mechanisms of TADF and phosphorescent materials. The microsecond or millisecond decay time of these scintillators may lead

---

[a] *Key Laboratory of Advanced Carbon-Based Functional Materials (Fujian Province University), College of Chemistry, Fuzhou University, Fuzhou, 350116, P. R. China. E-mail: meijin_lin@fzu.edu.cn; fangxin@fzu.edu.cn*

[b] *College of Materials Science and Engineering, Fuzhou University, Fuzhou, 350116, P. R. China. E-mail: chm@fzu.edu.cn*

[c] *College of Zhicheng, Fuzhou University, Fuzhou, 350002, P. R. China*

† Electronic supplementary information (ESI) available: Experimental procedures, characterization, additional spectra and other relevant data. CCDC 2309717 and 2309718. For ESI and crystallographic data in CIF or other electronic format see DOI: **https://doi.org/10.1039/d4sc00735b**

to afterglow interference in instantaneous X-ray imaging, thereby to some extent affecting the imaging quality.

Through the methodology of co-crystal engineering, the preparation of organic scintillators containing halogens emerges as a straightforward and effective strategy for the rapid development of high-radiation luminescence with strong X-ray absorption capabilities.[1,17] Organic co-crystals represent single-phase materials in which two or more components are intricately combined in specific stoichiometric ratios through non-covalent bonding forces, including π–π interactions, hydrogen-bonding, halogen-bonding, and charge transfer (CT) interactions.[18,19] The introduction of a second component induces supramolecular interactions that impose constraints on the ordered arrangement of molecules, limiting their free rotation and enhancing interactions between orbitals. This leads to a reduction in the forbidden bandwidth, an increase in luminescence and an enhancement in the fluorescence quantum yields (Φ_f) of the system. Meanwhile, charge transfer between the donor and acceptor may potentially enhance the carrier transport efficiency of the material, thereby improving its scintillation performance.[20,21] Recently, Sun *et al.*[22,23] demonstrated the feasibility of this strategy through their report on the organic co-crystal BIC scintillator.

In this work, we synthesized a highly luminescent organic dye, 2,5-di(pyridin-4-yl)thiazolo[5,4-*d*]thiazole (Py_2TTz), which was subsequently co-crystallized with 1,4-diiodotetrafluorobenzene (I_2F_4B) and 1,3,5-trifluoro-2,4,6-triiodobenzene (I_3F_3B), yielding two organic fluorophore co-crystals, denoted as $Py_2TTz–I_2F_4$ and $Py_2TTz–I_3F_3$ (Fig. 1b). Comprehensive testing revealed that $Py_2TTz–I_2F_4$ exhibited exceptional performance, distinguishing itself as a noteworthy organic co-crystal scintillator. It exhibits an ultrafast decay time of 1.426 ns, a high X-ray RL intensity (1.46 times higher than $Bi_3Ge_4O_{12}$) and a low detection limit of 70.49 nGy s^{-1}, representing 1/78th of the detection limit for medical applications (5.5 μGy s^{-1}). The formation of halogen-bonding in organic co-crystals restricts intermolecular rotation and reduces the probability of non-radiative leaps, thereby contributing to excellent scintillation properties.[24,25] Organic co-crystals induced by halogen bonds also have higher charge transfer efficiency. Furthermore, a flexible X-ray film prepared based on $Py_2TTz–I_2F_4$ achieved a high spatial resolution of 26.8 lp per mm at modulation transfer function (MTF) = 0.2 by the slanted edge method. It opens up new avenues for subsequent medical and industrial probes.

Results and discussion

Our approach involves employing the molecular self-assembly of organic ligands with iodine-based fluorophores (IFBs) to restrict intermolecular rotation through the supramolecular interactions of halogen-bonding, thereby reducing the non-radiative transition behavior of excitons. Prior to self-assembly, we assessed the strength of the intermolecular interactions within the organic co-crystals using molecular classical electrostatic surface potential (ESP).[26] The ESP values for compounds Py_2TTz, I_2F_4B and I_3F_3B were calculated using Multiwfn software (Fig. 1a).[27] For compound Py_2TTz, the minimum ESP is situated at the N atom, approximately −34.72 kcal mol^{-1}, whereas for I_2F_4B and I_3F_3B, the maximum

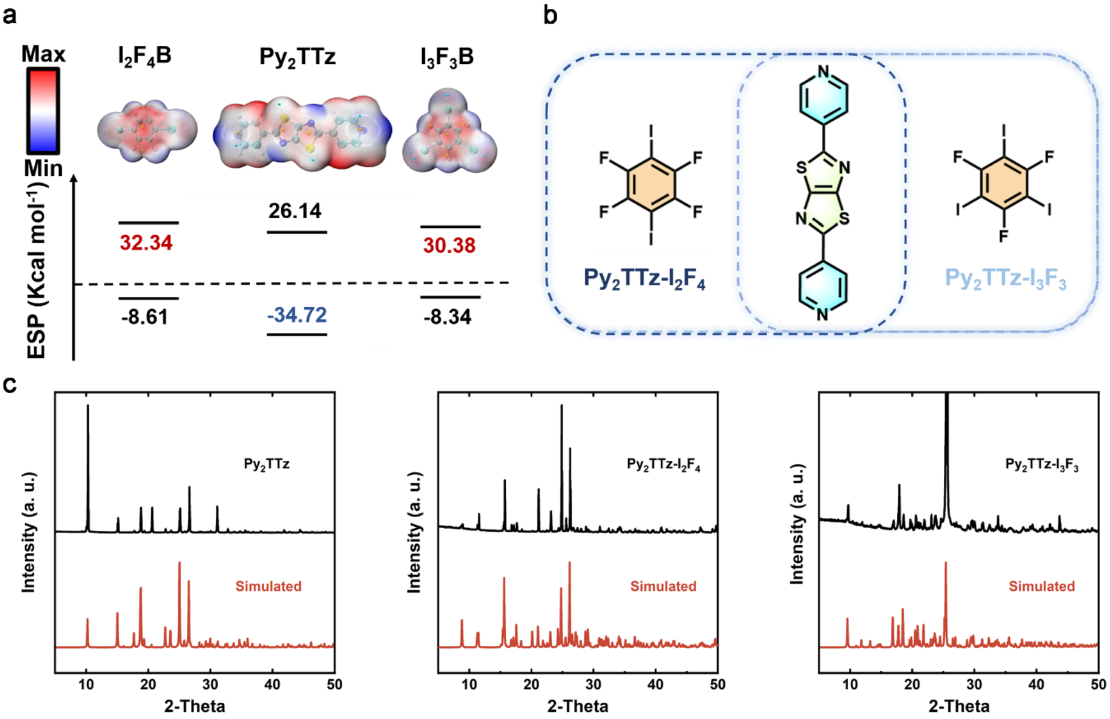

Fig. 1 (a) Calculated molecular electrostatic surface potential (ESP) visualization and extreme values for Py_2TTz, I_2F_4B, and I_3F_3B. (b) Chemical structures of $Py_2TTz–I_2F_4$ and $Py_2TTz–I_3F_3$. (c) XRD patterns of Py_2TTz, $Py_2TTz–I_2F_4$ and $Py_2TTz–I_3F_3$ crystalline powders compared with simulated XRD patterns.

ESP is observed near the I and F atoms, approximately 32.34 kcal mol^{-1}, 30.38 kcal mol^{-1}, respectively. The complete ESP extremes and corresponding spatial locations are given in Tables S1, S2 and S3.† The notable difference in ESP values between the donor N and acceptor I and F atoms suggests that, when these components come into contact in a solution environment, weak intermolecular interactions facilitate the rapid assembly of isolated molecules.

The synthesis of Py_2TTz and the crystal growth methods employed for $Py_2TTz–I_2F_4$ and $Py_2TTz–I_3F_3$ are detailed in the ESI.† [28,29] Considering the molar ratios of nitrogen in pyridine within Py_2TTz and iodine in halobenzene, initially mixed in a 1 : 1 ratio (Fig. 1b), the co-crystallization of Py_2TTz with I_2F_4B at a 1 : 1 assembly ratio and I_3F_3B at a 1 : 2 assembly ratio was achieved through the interactions of halogen-bonding and π–π stacking in organic crystals $Py_2TTz–I_2F_4$ and $Py_2TTz–I_3F_3$. The corresponding crystal structure parameters were determined through X-ray single-crystal diffraction analysis, as presented in Table S4.† Powder and single crystal X-ray diffraction patterns were utilized to assess the structural integrity of the series compounds. The observed diffraction peaks were found to align well with those simulated based on the single crystal diffraction structures (single crystal ccdc no. 2309717, no. 2309718), thereby confirming the purity of the series compound samples (Fig. 1c).

To assess the scintillator properties of the synthesized materials, radioluminescence spectra for these compounds were measured at an X-ray dose rate of 278 μGy s^{-1}, with $Bi_3Ge_4O_{12}$ (BGO) serving as the commercial reference material. Fig. 2a illustrates the X-ray excited luminescence mechanism of organic halogen co-crystal scintillators. As can be seen in

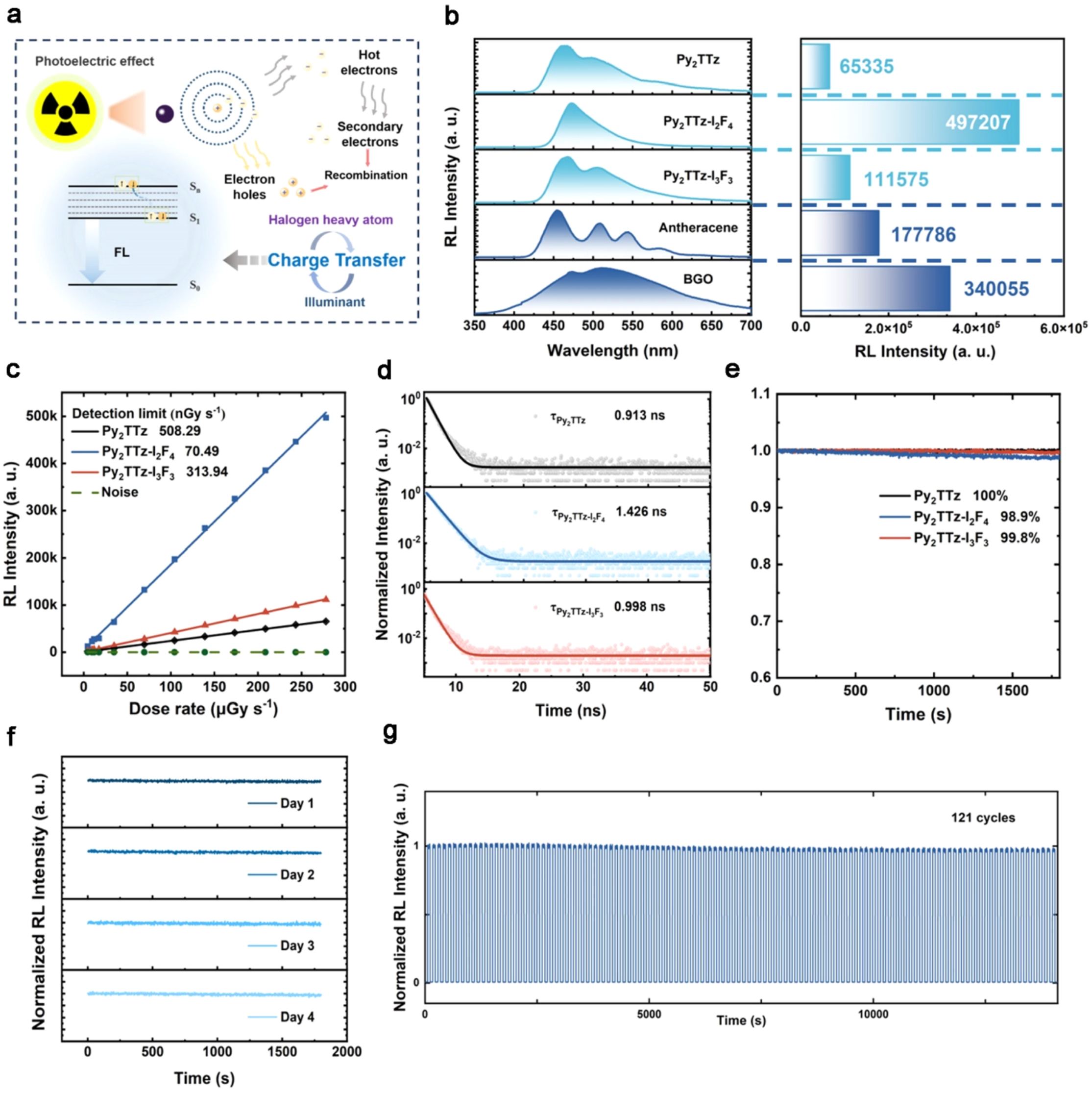

Fig. 2 (a) Schematic diagram of X-ray excited luminescence. (b)–(g) The scintillation properties of Py_2TTz, $Py_2TTz–I_2F_4$, $Py_2TTz–I_3F_3$, anthracene and $Bi_4Ge_3O_{12}$ (BGO) crystalline powders: (b) the RL spectra and the corresponding maximum RL intensity under the X-ray dose rate at 278 μGy s^{-1} (50 kV, 79 μA). (c) The linear fitting of the maximum RL intensity from 4.58 μGy s^{-1} to 278 μGy s^{-1}, the detection limits calculated by using the 3σ/slope. (d) The fitted curves of fluorescence lifetime decay under 450 nm excitation. (e) The irradiation stability under continuous irradiation (1800 s) for Py_2TTz, $Py_2TTz–I_2F_4$ and $Py_2TTz–I_3F_3$ powders under the X-ray dose rate at 278 μGy s^{-1}. For $Py_2TTz–I_2F_4$: (f) comparison of decreasing trends for 4 days of continuous irradiation, 30 minutes per day; (g) repeat 121 on–off cycles of the X-ray dose rate at 278 μGy s^{-1}.

Fig. 2b, the emission peaks for Py_2TTz, $Py_2TTz–I_2F_4$ and $Py_2TTz–I_3F_3$ were observed at 464 nm, 472 nm and 468 nm, respectively, with full-width at half-maximum (FWHM) values of approximately 87 nm, 52 nm and 88 nm. Notably, the FWHM of $Py_2TTz–I_2F_4$ was considerably narrower than those of conventional inorganic scintillators. In a preliminary assessment of scintillation properties, it is noteworthy that the RL intensity of $Py_2TTz–I_2F_4$ and $Py_2TTz–I_3F_3$ was significantly enhanced to 4.97×10^5 a. u. and 1.12×10^5 a. u., representing a 7.61-fold and 1.71-fold increase compared to Py_2TTz. When compared to the RL intensity of the commercial material BGO (3.40×10^5 a. u.)—irradiated at the same X-ray dose rate, the RL intensity of $Py_2TTz–I_2F_4$ was approximately 1.46 times higher. On this basis, we calculated the relative light yields of the materials. When the X-ray energy is 60 keV and the thickness of the sample is 0.1 cm, the X-ray attenuation efficiencies of Py_2TTz, $Py_2TTz–I_2F_4$ and $Py_2TTz–I_3F_3$ are 3.49%, 46.74% and 57.53%, respectively (Fig. S2†). It was indicated that the I_xF_xB component could effectively increase the X-ray absorption ability of the assembled co-crystals. Compared with reference anthracene (15 900 photons per MeV), the calibrated relative light yields of Py_2TTz, $Py_2TTz–I_2F_4$ and $Py_2TTz–I_3F_3$ are 7843, 32 583 and 11 354 photons per MeV, respectively.[15,30,31]

Fig. S3a–c† present the RL spectra at X-ray dose rates ranging from 4.58 to 278 μGy s^{-1}. These spectra exhibit a linear increase with the augmentation of X-ray dose rates (Table S5† provides the corresponding X-ray dose rates at specific currents and voltages). The detection limit for compound $Py_2TTz–I_2F_4$, determined using the 3σ method, is calculated to be 70.49 nGy s^{-1} (Fig. 2c), which is much lower than the values of Py_2TTz (508.29 nGy s^{-1}) and $Py_2TTz–I_3F_3$ (313.94 nGy s^{-1}).[14] Notably, this value is only 1/78th of the commonly employed X-ray diagnostic dose rate (5.5 μGy s^{-1}),[32] indicating its significant suitability for subsequent low-dose-rate X-ray imaging. Besides, these compounds exhibited ultra-short decay time as small as 0.913 ns (Py_2TTz), 1.426 ns ($Py_2TTz–I_2F_4$), and 0.998 ns ($Py_2TTz–I_3F_3$) (Fig. 2d and Table S6†), which can eliminate afterglow interference during transient imaging with X-rays.

Furthermore, the irradiation stability of compounds Py_2TTz, $Py_2TTz–I_2F_4$ and $Py_2TTz–I_3F_3$ was investigated (Fig. 2e). The samples retained nearly 100%, 98.9%, and 99.8% RL intensity following 1800 seconds of irradiation at an X-ray dose rate of 278 μGy s^{-1}. Concurrently, $Py_2TTz–I_2F_4$ underwent X-ray irradiation at the same dose rate for 30 minutes per day over four days, and the normalized data (Fig. 2f) revealed a consistent decreasing trend similar to that observed on the first day and at the onset. By raising the total dose to 14.42 Gy_{air}, (irradiation for 9832.5 s at a dose of 1467 μGy s^{-1}), the stability of $Py_2TTz–I_2F_4$ decreased to 82.7% of the original (Fig. S4†). In addition, stability was maintained under repeated completion of 121 switching cycles (Fig. 2g). This suggests that, even with the addition of a second ligand, the intermolecular interactions within the co-crystal exhibit resilience against deterioration after exposure to high-energy X-ray irradiation. Additionally, X-ray diffraction (XRD) characterization of the irradiated Py_2TTz, $Py_2TTz–I_2F_4$ and $Py_2TTz–I_3F_3$ indicated that molecular crystal structures remained essentially unchanged when compared to those observed before irradiation (Fig. S5†). Comprehensive details of all scintillator performance values are provided in Table S7.† In summarizing the scintillator properties of these materials, it is evident that, when compared to compounds Py_2TTz and BGO, compound $Py_2TTz–I_2F_4$ manifests higher RL intensity, a narrower FWHM value, and the lowest detection limit.

The RL intensity of organic fluorescent scintillators is positively correlated with the X-ray absorption efficiency (Abs), the fluorescence quantum yield (PLQY; Φ_f) and the carrier transport efficiency (η).[9,12,13] As shown in Fig. 3a, compounds $Py_2TTz–I_2F_4$ and $Py_2TTz–I_3F_3$ demonstrate higher X-ray absorption efficiency compared to compound Py_2TTz. Besides, Fig. 3b illustrates a sequential increase in Φ_f for compounds Py_2TTz, $Py_2TTz–I_3F_3$ and $Py_2TTz–I_2F_4$, reaching values of 12.09%, 15.92% and 18.85%, respectively. The incorporation of the second ligand enhances the Φ_f, which increases in a ratio proportional to the RL intensity. These findings indicate that the incorporation of a second monomer containing heavy atoms enhances both the X-ray absorption coefficient and Φ_f of organic co-crystals, resulting in a substantial improvement in scintillation performance.

In addition, we fabricated photoconductive devices of the three materials, the device simulations are shown in Fig. 3c, the complete fabrication details are shown in the ESI† and the actual photos of the devices are shown in Fig. S6.† And we tested their photoconductive properties at 30 V, 200 μA (X-ray dose rate of 2.765 mGy s^{-1}), respectively. Combined with the single-crystal size calculation, we obtained the maximum photocurrent densities of the devices. The maximum photocurrent densities of Py_2TTz, $Py_2TTz–I_2F_4$ and $Py_2TTz–I_3F_3$ are 4.51×10^{-3} nA mm^{-2}, 1.59×10^{-2} nA mm^{-2} and 9.60×10^{-3} nA mm^{-2}, respectively. The maximum photocurrent densities of $Py_2TTz–I_2F_4$ and $Py_2TTz–I_3F_3$ are 3.37 and 2.13 times higher

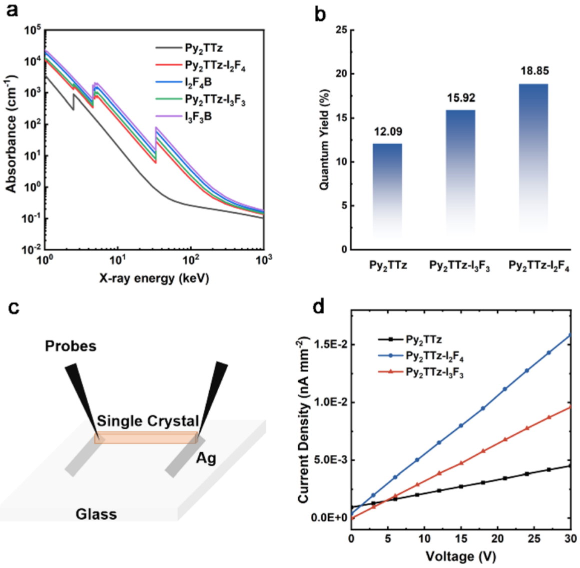

Fig. 3 (a) The X-ray energy-dependent absorption spectra of Py_2TTz, $Py_2TTz–I_2F_4$, $Py_2TTz–I_3F_3$, I_2F_4B and I_3F_3B. (b) The PLQY of Py_2TTz, $Py_2TTz–I_2F_4$ and $Py_2TTz–I_3F_3$. (c) Schematic of a photoconductive device based on Py_2TTz, $Py_2TTz–I_2F_4$ and $Py_2TTz–I_3F_3$ single crystals. (d) The photocurrent density *versus* voltage of the devices under the X-ray dose rate of 2.765 mGy s^{-1} (30 kV, 200 μA).

than that of Py_2TTz respectively. Meanwhile, the photocurrent density of $Py_2TTz–I_2F_4$ is 1.66 times higher than that of $Py_2TTz–I_3F_3$, which indicates that the X-ray excitation conductivity of $Py_2TTz–I_2F_4$ is the best. Therefore, due to the highest fluorescence quantum yield and maximum X-ray-excited photocurrent, $Py_2TTz–I_2F_4$ exhibits the most outstanding radioluminescent performance among these three materials.[13,33,34]

Given the profound influence of single crystal structures on their solid-state luminescence properties and conductivity under X-ray exposure, we investigated the molecular crystal structures of these compounds and the accuracy of the theoretical calculations was confirmed. Theoretical calculations indicate that different charge transport phenomena occur, induced by supramolecular interactions (including π–π interactions and halogen-bonding), when the positional orientations of the iodine-based fluorophore (I_xF_xB) and Py_2TTz are varied, which affects the current under X-ray exposure. When the I_xF_xB is located on the longitudinal axis of Py_2TTz, the main supramolecular interactions are caused by π–π stacking and the electrons in co-crystals are all on Py_2TTz without charge separation (Fig. 4a and b, left). Although π–π stacking improves conductivity substantially, theoretical calculations have shown that it cannot be formed. In contrast, when the I_xF_xB is located on the transverse axis of Py_2TTz, the main supramolecular interactions are induced by halogen bonding. Most of the electrons in the HOMO orbitals are distributed on the iodine-based fluorophore, whereas the electrons in the LUMO orbitals are distributed on Py_2TTz, which suggests that the halogen-bonding-induced charge-transfer co-crystal has been formed (Fig. 4a and b, right).[35] On one hand, the charge transport induced by head-to-head halogen bonding increases the conductivity, and on the other hand it limits the molecular rotation and improves the luminescence properties of the co-crystal. The stacking patterns predicted by theoretical calculations are consistent with the ESP results.

On the basis of theoretical calculations, we analyzed the single crystal structures in depth. In contrast to compound Py_2TTz, which crystallizes in the monoclinic $P2_1/c$ space group, both compounds $Py_2TTz–I_2F_4$ and $Py_2TTz–I_3F_3$ crystallize in the triclinic $P\bar{1}$ space group. The cell parameters for compound $Py_2TTz–I_2F_4$ are $a = 6.2882$ Å, $b = 8.7402$ Å, $c = 11.0715$ Å, $\alpha = 106.876°$, $\beta = 102.839°$, $\gamma = 105.122°$; the cell parameters for $Py_2TTz–I_3F_3$ are $a = 7.7556$ Å, $b = 8.7408$ Å, $c = 18.7834$ Å, $\alpha = 84.004°$, $\beta = 79.941°$, $\gamma = 67.184°$ (Table S4†). As can be seen in Fig. 4c, the packing arrangement of crystal Py_2TTz reveals that it is arranged in a staggered parallel orientation. Upon three-dimensional packing, the pyridine heads and tails on Py_2TTz overlap in parallel between adjacent faces. The distance from the pyridine ring to the adjacent plane is 3.3453 Å. To analyze the alterations post-addition of I_2F_4B, the packing of crystal $Py_2TTz–I_2F_4$ is presented as a stepped arrangement in the one-dimensional direction. The Py_2TTz molecules in the co-crystal are positioned as left and right neighbours without face-to-face stacking. Notably, halogen-bonding interactions exist between the N on the pyridine in Py_2TTz and I of I_2F_4B ($d_{C–I\cdots N} = 2.8688$ Å). Following three-dimensional packing, similar to crystal

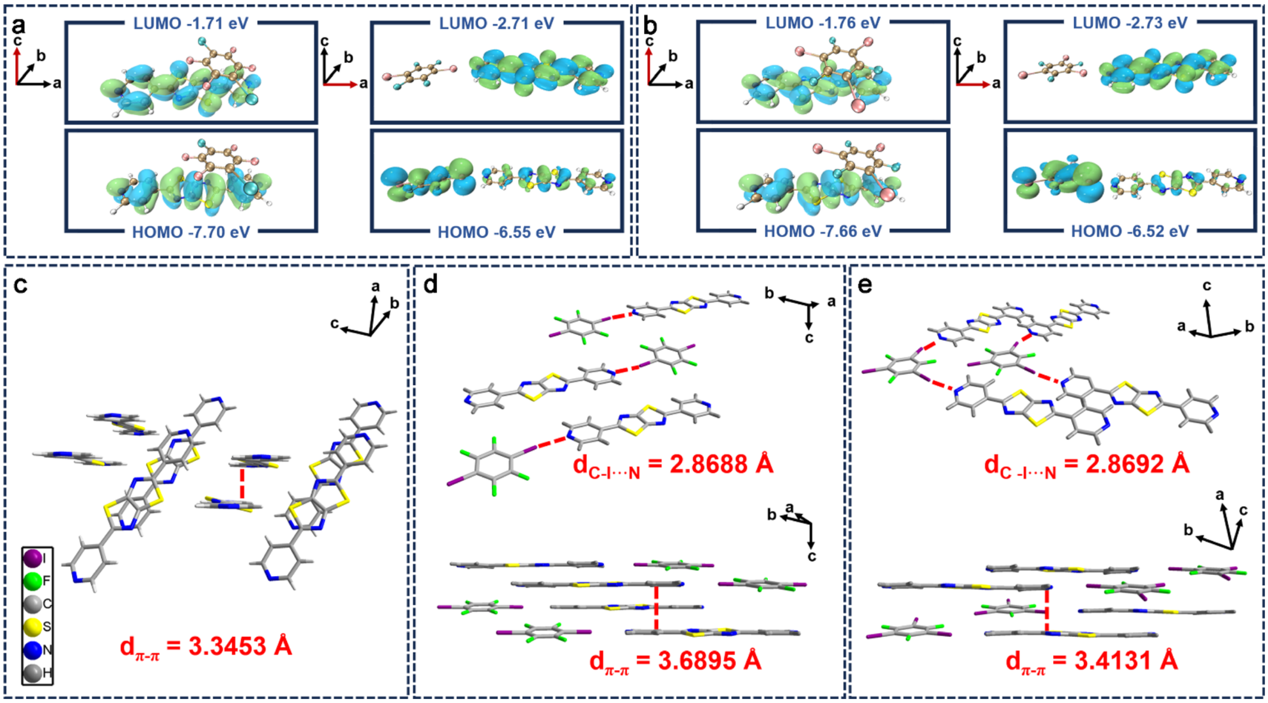

Fig. 4 (a) Calculated orbital energy levels of $Py_2TTz–I_2F_4$ (longitudinal axis, left; transverse axis, right). (b) Calculated orbital energy levels of $Py_2TTz–I_3F_3$ (longitudinal axis, left; transverse axis, right). (c) The packing of Py_2TTz in the three-dimensional direction (the π–π interactions). (d) The packing of $Py_2TTz–I_2F_4$ in the one-dimensional direction (the halogen-bonding interactions) and the packing of the crystal in the three-dimensional direction (the π–π interactions). (e) The packing of $Py_2TTz–I_3F_3$ in the one-dimensional direction (the halogen-bonding interactions) and the packing of the crystal in the three-dimensional direction (the π–π interactions).

Py_2TTz, the distance from the pyridine ring to the adjacent plane π–π interaction is 3.6895 Å (Fig. 4d), while for crystal $Py_2TTz–I_3F_3$, halogen-bonding interactions within the one-dimensional plane are observed at $d_{C–I\cdots N} = 2.8692$ Å, forming a triangular alignment. The three-dimensional packing mirrors a configuration similar to crystal $Py_2TTz–I_2F_4$, with the distance from the pyridine ring to the adjacent plane measuring 3.4131 Å (Fig. 4e). The weakest π–π interaction of crystal $Py_2TTz–I_2F_4$ partially mitigates the impact of fluorescence quenching, increasing the fluorescence quantum yields. Simultaneously, the presence of stronger halogen-bonding enhances intermolecular interactions and the formation of halogen-bond-induced charge-transfer separated states of the donor–acceptor improves the carrier transport efficiency, thus realizing an enhancement of the conductivity under X-ray exposure. Details of the weak interactions are provided in Fig. S7 and S8†.

Additionally, the intermolecular interactions in the vicinity of the Py_2TTz, following the addition of I_2F_4B and I_3F_3B, were systematically investigated. The Hirshfeld surfaces of the three materials were computed and analyzed using CrystalExplorer software, where red areas denote strong intermolecular interactions, and other areas represent weak intermolecular interactions.[37,38] As can be seen in Fig. S9,† a color-comparison of the Hirshfeld surfaces revealed that the original Py_2TTz molecule exhibited red color only near the hydrogen on pyridine. However, upon the incorporation of I_2F_4B and I_3F_3B, a broader range of red color near the pyridine nitrogen on the Py_2TTz molecule was observed, consistent with the prediction from previous ESP data. Meanwhile, the relative contributions of various weak interactions outside Py_2TTz were further elucidated from the 2D fingerprints plotted by CrystalExplorer. As can be seen from the pie charts in Fig. S10,† the incorporation of the second ligand in the co-crystal enriched the weak interactions in the vicinity of Py_2TTz. Since the unit assembly ratio of $Py_2TTz–I_3F_3$ is 1 : 2, the halogen-bonding ratio is higher than that of $Py_2TTz–I_2F_4$ with the unit assembly ratio of 1 : 1. Combined with the weak interactions shown in Fig. S7 and S8,† the presence of halogen and hydrogen bonds restricts the free rotation of molecules, resulting in more compact molecular packing. The blockade of nonradiative channels can further inhibit fluorescence quenching, thereby reducing non-radiative transition rates and ensuring a higher PLQY value.[12,13] Calculations of the non-radiative transition rates can support the above point. The k_{nr} values are 5.69×10^8 s^{-1} ($Py_2TTz–I_2F_4$), 8.42×10^8 s^{-1} ($Py_2TTz–I_3F_3$) and 9.63×10^8 s^{-1} (Py_2TTz), in increasing order.[39] The difference in the nonradiative transition rates further illustrates that the RL performance of $Py_2TTz–I_3F_3$ is not as good as that of $Py_2TTz–I_2F_4$.

Leveraging the outstanding scintillation properties of compound $Py_2TTz–I_2F_4$, we proceeded to apply it in X-ray

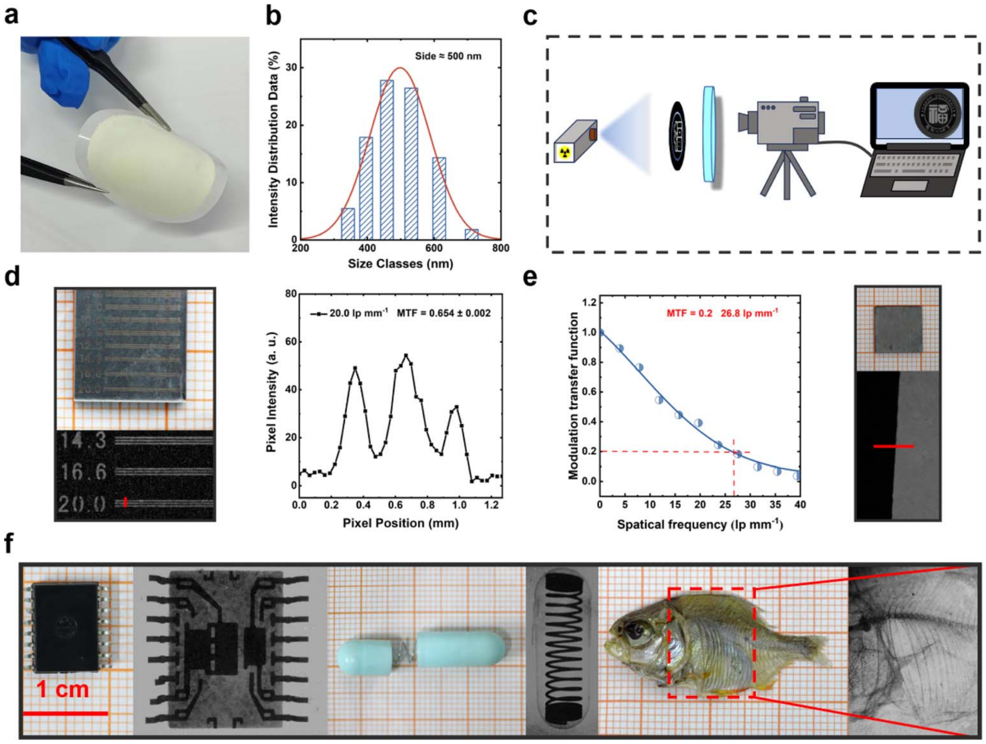

Fig. 5 (a) Flexibility testing in natural light of $Py_2TTz–I_2F_4$ (PET). (b) Particle size measured by dynamic light scattering. (c) A schematic diagram of the X-ray imaging. (d) The X-ray exposure contrast images of the line-pair card (type 25N: 3.5–20 lp per mm) and the pixel intensity *versus* pixel positions (resolution = 20 lp per mm MTF = 0.654 ± 0.002) under X-ray exposure. (e) The X-ray exposure contrast images of the tungsten sheet and the MTF *versus* actual line-pair measured by the slanted edge method (resolution = 26.8 lp per mm, MTF = 0.2) under X-ray exposure. (f) The X-ray exposure contrast photographs of: the electronic component with complex internal structures (left), a capsule containing a metallic spring (middle) and biological imaging of a fish (right).

Table 1 Performance comparison of organic scintillators for X-ray imaging in the literature[a]

				X-ray imaging		
Materials	LOD (nGy s^{-1})	Decay time	Stability	Composition	Resolution (lp per mm)	Reference
9.10-DPA	14.3	1.63 ns	94%	Single crystal	20.0	2021 (ref. 8)
DMAc–TRZ	103.2	20 ns, 2.15 μs	Nearly unchanged	0.5 wt% in SO	16.6	2022 (ref. 15)
O-ITC	33	46.5 ms	94%	Powder in PDMS	—	2021 (ref. 14)
BIC	85	2.71 ns	93%	5 wt% in PDMS	16.7	2023 (ref. 22)
PNP-A	566	830.5 ms	Nearly unchanged	PDMS	11.25	2023 (ref. 36)
CBP	25.5	1.15 ns	99.2%	PDMS	14.3	2023 (ref. 9)
BPA–Br	25.95	8.25 ns	98.5%	100 wt% in PTFE	14.3–20.0	2023 (ref. 13)
$Py_2TTz–I_2F_4$	117.97	1.44 ns	98.9%	100 wt% in PET	26.8	This work

[a] Stability is defined as the ratio of the RL intensity after irradiation to the initial intensity. Testing conditions are described in Table S8.

imaging. First, the co-crystal was ball-milled for 4 hours in the antisolvent (water). The RL spectrum and PXRD post-ball-milling are depicted in Fig. S11 and S12.† Following ball milling, the RL waveform remained unchanged, and an intensity value of 1.28×10^5 a. u. was achieved. A comparison with the PXRD spectrum revealed the disappearance of some crystalline peaks attributable to the ball milling process. This could be a contributing factor to the observed reduction in the radiation luminescence properties of the material. The particle size of the powder post-ball-milled was determined to be approximately 500 nm (Fig. 5b). The PET polyester microporous filter membrane with a pore size of 0.45 μm was selected, and the ball-milled sample was pump-filtered on a PET film to obtain a flexible film of an adsorbed sample (Fig. S13†). Detailed preparation procedures are described in the ESI.†

By placing the sample between the X-ray source and the item to be imaged and photographing it with a commercial digital camera (Fig. 5c), we successfully acquired X-ray images of the sample. As shown in Fig. 5d (left) and S14,† there are clear boundaries between light and dark at 20 lp per mm and in the range of 25–30 lp per mm. In this case, a curve of pixel *versus* pixel position in the plots was obtained using ImageJ software.[40] The light and dark line pairs of 20.0 lp per mm on the line-pair card were observed at MTF = 0.654 ± 0.002 (Fig. 5d, right).[41] Besides, measured by the slanted edge method,[42,43] the actual spatial resolution was found to be 26.8 lp per mm at MTF = 0.2 (Fig. 5e), and details of the edge method are provided in the ESI.† Furthermore, the X-ray images portraying the intricate structures within an electronic component are presented in Fig. 5f, providing the clear visualization of the spring inside a capsule and revealing the distinct internal structure of a dried fish. These findings suggest that $Py_2TTz–I_2F_4$ holds considerable potential for using as a flexible X-ray detector in industrial and biological imaging applications (Table 1).

Conclusions

In summary, we have obtained an example of an organic co-crystal scintillator, $Py_2TTz–I_2F_4$, characterized by rapid response and outstanding X-ray imaging performance. Its crystalline powders exhibited a high X-ray RL intensity (approximately 1.46 times higher than that of BGO), a low detection limit of 70.49 nGy s^{-1}, a narrow FWHM of 52 nm and an ultrafast decay time of 1.426 ns. As an organic co-crystal scintillator, it demonstrates excellent irradiation stability. The incorporation of IFBs overcomes the problems of low X-ray absorption efficiency of organic scintillators. Halogen-bond-induced charge-transfer co-crystals were formed to achieve higher X-ray excitation conductivity. The flexible scintillator film produced by the suction filtration method had shown great potential in X-ray imaging, which obtains the light and dark line pairs of 20.0 lp per mm on the line-pair card at MTF = 0.654 ± 0.002. Further measuring by the slanted edge method, the spatial resolution can reach 26.8 lp per mm at MTF = 0.2. Based on our knowledge, this material represents the organic co-crystal scintillator with the shortest decay time and the best imaging effect.

Data availability

All data are available in the manuscript and in the ESl.†

Author contributions

Y.-H. Chen completed the experiments and wrote the manuscript, G.-Z. Zhang assisted in the imaging measurements, and F.-H. Chen helped the theoretical calculations. S.-Q. Zhang contributed to the interpretation of the experimental results. M.-J. Lin, H.-M. Chen and X. Fang supervised and revised the manuscript. All authors discussed the results and commented on the manuscript.

Conflicts of interest

There are no conflicts to declare.

Acknowledgements

This work was supported by the National Natural Science Foundation of China (22201042 and 22371047), Natural Science

Foundation of Fujian Province (2022J05118 and 2023J01425), Collaborative Innovation Platform Project of Fu-Xia-Quan National Independent Innovation Demonstration Zone (2022-P-021) and Fuzhou Science and Technology (2022-P-001).

Notes and references

1 Y. Zhou, J. Chen, O. M. Bakr and O. F. Mohammed, *ACS Energy Lett.*, 2021, **6**, 739–768.
2 Z. Lin, S. Lv, Z. Yang, J. Qiu and S. Zhou, *Adv. Sci.*, 2021, **9**, 2102439.
3 C. Cao, M. F. Toney, T.-K. Sham, R. Harder, P. R. Shearing, X. Xiao and J. Wang, *Mater. Today*, 2020, **34**, 132–147.
4 Z. Hong, Z. Chen, Q. Chen and H. Yang, *Acc. Chem. Res.*, 2022, **56**, 37–51.
5 M. Chen, C. Wang and W. Hu, *J. Mater. Chem. C*, 2021, **9**, 4709–4729.
6 Y. Wang, M. Li, Z. Chai, Y. Wang and S. Wang, *Angew. Chem., Int. Ed.*, 2023, **62**, e202304638.
7 H. Wu, Y. Ge, G. Niu and J. Tang, *Matter*, 2021, **4**, 144–163.
8 M. Chen, L. Sun, X. Ou, H. Yang, X. Liu, H. Dong, W. Hu and X. Duan, *Adv. Mater.*, 2021, **33**, e2104749.
9 H. Chen, M. Lin, C. Zhao, D. Zhang, Y. Zhang, F. Chen, Y. Chen, X. Fang, Q. Liao, H. Meng and M. Lin, *Adv. Opt. Mater.*, 2023, **11**, 2300365.
10 J.-X. Wang, Y. Wang, I. Nadinov, J. Yin, L. Gutiérrez-Arzaluz, O. Alkhazragi, T. He, T. K. Ng, M. Eddaoudi, H. N. Alshareef, O. M. Bakr, B. S. Ooi and O. F. Mohammed, *ACS Mater. Lett.*, 2022, **4**, 1668–1675.
11 T. J. Hajagos, C. Liu, N. J. Cherepy and Q. Pei, *Adv. Mater.*, 2018, **30**, 1706956.
12 X. Wang, G. Niu, Z. Zhou, Z. Song, K. Qin, X. Yao, Z. Yang, X. Wang, H. Wang, Z. Liu, C. Yin, H. Ma, K. Shen, H. Shi, J. Yin, Q. Chen, Z. An and W. Huang, *Research*, 2023, **6**, 0090.
13 H. Chen, M. Lin, Y. Zhu, D. Zhang, J. Chen, Q. Wei, S. Yuan, Y. Liao, F. Chen, Y. Chen, M. Lin and X. Fang, *Small*, 2023, 2307277.
14 X. Wang, H. Shi, H. Ma, W. Ye, L. Song, J. Zan, X. Yao, X. Ou, G. Yang, Z. Zhao, M. Singh, C. Lin, H. Wang, W. Jia, Q. Wang, J. Zhi, C. Dong, X. Jiang, Y. Tang, X. Xie, Y. Yang, J. Wang, Q. Chen, Y. Wang, H. Yang, G. Zhang, Z. An, X. Liu and W. Huang, *Nat. Photonics*, 2021, **15**, 187–192.
15 W. Ma, Y. Su, Q. Zhang, C. Deng, L. Pasquali, W. Zhu, Y. Tian, P. Ran, Z. Chen, G. Yang, G. Liang, T. Liu, H. Zhu, P. Huang, H. Zhong, K. Wang, S. Peng, J. Xia, H. Liu, X. Liu and Y. M. Yang, *Nat. Mater.*, 2022, **21**, 210–216.
16 J.-X. Wang, L. Gutiérrez-Arzaluz, X. Wang, T. He, Y. Zhang, M. Eddaoudi, O. M. Bakr and O. F. Mohammed, *Nat. Photonics*, 2022, **16**, 869–875.
17 L. Bai, P. Bose, Q. Gao, Y. Li, R. Ganguly and Y. Zhao, *J. Am. Chem. Soc.*, 2017, **139**, 436–441.
18 Y. Huang, Z. Wang, Z. Chen and Q. Zhang, *Angew. Chem., Int. Ed.*, 2019, **58**, 9696–9711.
19 J. Lieffrig, O. Jeannin, K.-S. Shin, P. Auban-Senzier and M. Fourmigué, *Crystals*, 2012, **2**, 327–337.
20 C. Z. Liu, S. Koppireddi, H. Wang, D. W. Zhang and Z. T. Li, *Angew. Chem., Int. Ed.*, 2018, **58**, 226–230.
21 J. C. Christopherson, F. Topić, C. J. Barrett and T. Friščić, *Cryst. Growth Des.*, 2018, **18**, 1245–1259.
22 Q. Sun, H. Wang, J. L. Li, F. L. Li, W. Zhu, X. Zhang, Q. Chen, H. Yang and W. Hu, *Small Struct.*, 2023, **4**, 2200275.
23 W. Zhu, R. Zheng, Y. Zhen, Z. Yu, H. Dong, H. Fu, Q. Shi and W. Hu, *J. Am. Chem. Soc.*, 2015, **137**, 11038–11046.
24 W. Wang, Y. Zhang and W. J. Jin, *Coord. Chem. Rev.*, 2020, **404**, 213107.
25 P. Xu, Q. Qiu, X. Ye, M. Wei, W. Xi, H. Feng and Z. Qian, *Chem. Commun.*, 2019, **55**, 14938–14941.
26 H. Jain, D. Sutradhar, S. Roy and G. R. Desiraju, *Angew. Chem., Int. Ed.*, 2021, **60**, 12841–12846.
27 T. Lu and F. Chen, *J. Comput. Chem.*, 2011, **33**, 580–592.
28 M. Ghora, P. Majumdar, M. Anas and S. Varghese, *Chem.–Eur. J.*, 2020, **26**, 14488–14495.
29 A. N. Woodward, J. M. Kolesar, S. R. Hall, N. A. Saleh, D. S. Jones and M. G. Walter, *J. Am. Chem. Soc.*, 2017, **139**, 8467–8473.
30 W. F. Wang, M. J. Xie, P. K. Wang, J. Lu, B. Y. Li, M. S. Wang, S. H. Wang, F. K. Zheng and G. C. Guo, *Angew. Chem., Int. Ed.*, 2024, **63**, e202318026.
31 S. Yuan, G. Zhang, F. Chen, J. Chen, Y. Zhang, Y. Di, Y. Chen, Y. Zhu, M. Lin and H. Chen, *Adv. Funct. Mater.*, 2024, 2400436.
32 H. Zhang, Z. Yang, M. Zhou, L. Zhao, T. Jiang, H. Yang, X. Yu, J. Qiu, Y. Yang and X. Xu, *Adv. Mater.*, 2021, **33**, 2102529.
33 C. Dong, X. Wang, W. Gong, W. Ma, M. Zhang, J. Li, Y. Zhang, Z. Zhou, Z. Yang, S. Qu, Q. Wang, Z. Zhao, G. Yang, A. Lv, H. Ma, Q. Chen, H. Shi, Y. Yang and Z. An, *Angew. Chem., Int. Ed.*, 2021, **60**, 27195–27200.
34 H. Chen, J. Chen, M. Li, M. You, Q. Chen, M. Lin and H. Yang, *Sci. China: Chem.*, 2022, **65**, 2338–2350.
35 J. Guo, L. Xu, M. Cai, Z. Dong, Q. Mu, X. Wang, H. Fan, F. Teng, X. He, H. Jiang and P. Hu, *Cryst. Growth Des.*, 2024, **24**, 1293–1301.
36 Y. Lei, G. Peng, Y. Xu, H. Wang, Z. Li and Z. Jin, *Adv. Opt. Mater.*, 2023, 2302068.
37 Z. Wu, J. Nitsch, J. Schuster, A. Friedrich, K. Edkins, M. Loebnitz, F. Dinkelbach, V. Stepanenko, F. Würthner, C. M. Marian, L. Ji and T. B. Marder, *Angew. Chem., Int. Ed.*, 2020, **59**, 17137–17144.
38 P. R. Spackman, M. J. Turner, J. J. McKinnon, S. K. Wolff, D. J. Grimwood, D. Jayatilaka and M. A. Spackman, *J. Appl. Crystallogr.*, 2021, **54**, 1006–1011.
39 Z. Xiong, X. Zhang, L. Liu, Q. Zhu, Z. Wang, H. Feng and Z. Qian, *Chem. Sci.*, 2021, **12**, 10710–10723.
40 R. Gerst, Z. Cseresnyés and M. T. Figge, *Nat. Methods*, 2023, **20**, 168–169.
41 L. J. Xu, X. Lin, Q. He, M. Worku and B. Ma, *Nat. Commun.*, 2020, **11**, 4329.
42 H. Zhang, C. Li and Y. Duan, *Optik*, 2018, **157**, 635–643.
43 K. Masaoka, *Opt. Express*, 2019, **27**, 1345–1352.